

Effect of Rashba spin-orbit coupling, magnetization and mixing of gap parameter on tunnelling conductance in F|NCSC junction of an F|S|F spin valve

Saumen Acharjee* and Umananda Dev Goswami†

Department of Physics, Dibrugarh University, Dibrugarh 786 004, Assam, India,

In this paper, we study the quantum transport at the Ferromagnet|Noncentrosymmetric Superconductor (F|NCSC) interface of an F|S|F spin valve. In this context, we investigate the tunneling conductance and its dependence on Rashba Spin-Orbit Coupling (RSOC) considering different barrier strength and a significant Fermi Wave-vector Mismatch (FWM) at the ferromagnetic and superconducting regions. The study is carried out for different magnetization orientations and its strength. We developed Bogoliubov de Gennes (BdG) Hamiltonian introducing RSOC and exchange interaction for such an hybrid structure. To study charge conductance we use an extended Blonder - Tinkham - Klapwijk (BTK) approach along with scattering matrix formalism to calculate the scattering coefficients. Our results strongly suggest that the tunneling conductance is strongly dependent on RSOC, magnetization strength, its orientation and the FWM. The work has also been done for different singlet-triplet mixing of the gap parameter. We have observed that with the rise of singlet-triplet mixing ratio the conductance decreases. It is also observed that a transparent barrier with moderate RSOC and having moderate magnetization strength with arbitrary orientation is highly suitable for maximum conductance.

PACS numbers: 67.30.hj, 85.75.-d, 74.90.+n

I. INTRODUCTION

During the last few decades many heavy fermion compounds have been discovered which shows unconventional superconductivity [1–28]. With the discovery of unconventional superconductivity, the study of quantum transport in Ferromagnet|Superconductor (F|S) hybrid structures and spin valves gain lots of attention during this period not only from the fundamental physics point of view but also from the applications purpose, as these heterostructure hold a great potential for the applications in the nano-technological spintronic devices. Tunneling spectroscopy at the F|S interface is found to be one of the most powerful tool to investigate the nature of the superconducting states. Over the years, the study reveals many information for both conventional as well as unconventional pairing symmetries in the superconductors. From the point of view of Cooper pairing, two symmetries have been found very important in superconducting state: the symmetry of inversion center and the time reversal. In absence of one of these, Cooper pairs will appear in an unconventional form. Although Noncentrosymmetric Superconductors (NCSC) are the candidate of prime concern over the last decade, the field received a significant boost only since the discovery of noncentrosymmetry in heavy fermion compound CePt₃Si [7–9]. Soon, many superconducting materials had been reported which lacks center of inversion [10–26]. A few of them are LaPt₃Si, UIr, La(Rh,Pt,Pd,Ir)Si₃, Li₂(Pt,Pd)₃B, Re₆Zr, LaNiC₂, Cd₂Re₂O₇, PbTaSe₂, etc. Due to the lack of center of symmetry, crystal structure induces an Antisymmetric Spin-Orbit Coupling (ASOC) and as a result parity no longer remains conserved. Consequently, the Fermi surface splits and the superconducting ground state exhibit an admixture of spin singlet and spin triplet components, if the pair-

ing gap is much smaller than the Spin-Orbit Coupling (SOC) strength.

With the rise of spintronics and the ability to use spin degree of freedom with much precision in recent times, the field of spintronics gains a lot of attention from the application point of view. SOC is considered to be the central point of the emergence of spintronics. Rashba Spin-Orbit Coupling (RSOC) is a special kind of SOC. Unlike Dirac coupling it arises in crystals due to the lack of inversion symmetry. Since, the inversion center is absent in NCSC, hence it possess ASOC. So, it becomes really important to understand the role of RSOC in quantum transport and consequent tunneling process.

The tunneling conductance and its dependence on the SOC [29–38] had been studied previously for different hybrid structures. Recent theoretical researches indicate that the ratio of spin singlet to the spin triplet pairing states in a superconductor is highly anticipated by the strength of the SOC. This theoretical predictions was later supported by experimental findings in [16–18] in heavy fermion compound Li₂(Pt,Pd)₃B. The experimental results showed that the pairing changes from spin-triplet state to spin-singlet state if Pt is replaced by Pd. Many other heavy fermion NCSC's had been studied since then and it was found that the pairing states were highly anticipated on strong SOC. Although conventional s-wave pairing [11, 39–42] is dominant in most cases, however it was also observed that the compounds with low spin-orbit coupling show unconventional superconductivity [22, 43–45]. Hence, in this regard it becomes necessary to investigate the role of SOC on the pairing of NCSC's.

It is known from the earlier works that the role of magnetization in F|S hybrid structures [46–58] is too significant. The transport properties and tunneling conductance in F|S (singlet) junction [46–48], F|S (triplet) junctions [49–53] and NCSC structures [54–56] have been studied earlier. However, the interplay of magnetization with RSOC and its effect on the tunneling conductance in F|NCSC hybrid structures is still unknown. Since NCSC consists of both triplet and singlet pairing states simultaneously, thus it is necessary to investigate the

*saumenacharjee@gmail.com

†umananda2@gmail.com

interplay of magnetization and the mixed pairing states (singlet and triplet) in NCSC's and their influence on conductance characteristics.

Motivated by the earlier works as mentioned above, in this work we investigate the effect of RSOC, magnetization and singlet-triplet mixing of gap parameter on the tunneling conductance due to the effect of these parameters on transport of an electron at the F|NCSC junction of an F|S|F spin valve.

The paper is organized as follows. In the Section II, a theoretical framework of the proposed setup is developed. The results of our work is discussed in the Section III. Finally we conclude our work in the Section IV.

II. THEORY

A. Model and formalism

We consider a F|S|F spin valve shown in Fig.1 consisting of a NCSC layer sandwiched between two ferromagnetic layers having different strength of magnetization. The left ferromagnetic layer is soft and can have any arbitrary orientation of magnetization, while the magnetization of the right ferromagnetic layer is fixed. In our analysis we choose that the orientation of the hard ferromagnetic layer is along the z-direction. We construct the Bogoliubov de-Gennes (BdG) Hamiltonian for the proposed setup and then solved the BdG equation at different interfaces to obtain the wave functions. The reflection and the transmission coefficients were then obtained by the proper choice of boundary conditions. In order to calculate the tunneling conductance at the F|NCSC interface of the F|S|F spin valve we use scattering matrix formalism to calculate the reflection and transmission coefficients and then by using an extended Blonder - Tinkham - Klapwijk (BTK) approach [59], we calculated the tunneling conductance at the F|NCSC junction of the valve.

The starting point of our theory is the Bogoliubov-de Gennes (BdG) equations, which can be read as

$$\mathcal{H}_{BdG}\Psi_{\alpha}(r) = E\Psi_{\alpha}(r), \quad (1)$$

where $\Psi_{\alpha}(r)$ is the Bogoliubov wave function has the following form:

$$\Psi_{\alpha}(r) = (u_{n\uparrow}, u_{n\downarrow}, v_{n\uparrow}, v_{n\downarrow})^T. \quad (2)$$

Here, u_n s and v_n s are basis functions representing the spin-up (\uparrow) and spin-down (\downarrow) states of electronlike and holelike quasiparticles respectively.

In matrix form the BdG Hamiltonian of the system can be written as

$$\mathcal{H}_{BdG} = \begin{pmatrix} \hat{H}_0 & \hat{\Delta}_{\alpha\beta}(r, r') \\ \hat{\Delta}_{\alpha\beta}^{\dagger}(r, r') & -\hat{H}_0^{\dagger} \end{pmatrix}_{4 \times 4}, \quad (3)$$

where the hat sign represents 2×2 matrices in spin space and \hat{H}_0 is the single particle Hamiltonian can be written as

$$\hat{H}_0 = \left(-\frac{\nabla^2}{2} - E_{Fi} + U_{int} \right) \hat{I} - \vec{h} \cdot \hat{\sigma}, \quad (4)$$

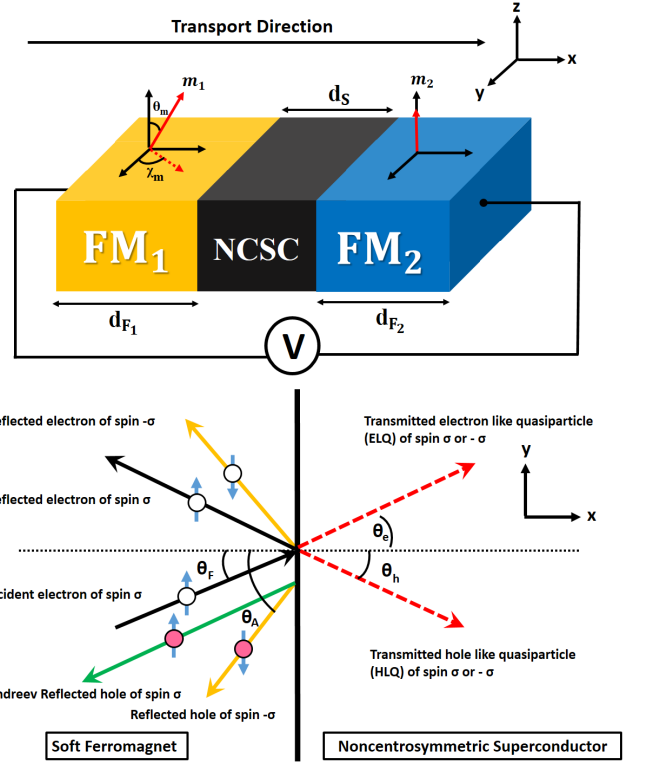


FIG. 1: The proposed experimental setup consists of noncentrosymmetric superconductor (NCSC) sandwiched between a soft and a hard ferromagnetic (FM) layers. The magnetization orientation of the soft and the hard FM layers are supposed to be misaligned by a polar angle θ_m and azimuthal angle χ_m as shown in the figure at top. The figure in the bottom gives a schematic overview of the scattering process takes place at the Ferromagnet|Noncentrosymmetric Superconductor (F|NCSC) junction. When an electron with spin up in the free FM region is incident on the F|NCSC interface there will be three possibilities: (i) it get reflected as a normal spin up electron, (ii) it gets retro-reflected as a hole with spin up or down configuration but in the opposite direction with the incident electron, and (iii) it gets transmitted in the S-region as a electron or hole like quasiparticle with up or down spin. Here, we assumed x-direction as the direction of transport. Different colours of the ferromagnetic layers indicates the level of magnetization.

where \hat{I} is the 2×2 unit matrix and $\hat{\sigma}$ are the Pauli matrices. The first term appearing in this equation represents the single particle kinetic energy, where for simplicity we consider $\hbar = 1$ and the electronic mass m as unity. E_{Fi} gives the Fermi energies in the respective layers. The ratio of square root of the Fermi energy in the superconducting layer E_{FS} to the Ferromagnetic layer E_{FF} is denoted by a dimensionless parameter λ , which physically represents Fermi Wave-vectors Mismatch (FWM) in the respective layers. That is, we define $\lambda = \sqrt{\frac{E_{FS}}{E_{FF}}} = \frac{q_{FS}}{k_{FF}}$, where q_{FS} and k_{FF} are the Fermi momentum in superconducting and ferromagnetic layers respectively. U_{int} gives the interaction potential of the F|NCSC interface located at $x = 0$ along the y direction. To study the

effect of RSOC, we consider our interaction potential U_{int} as follows [37, 38, 52, 60]:

$$U_{int}(x) = [U_0 + U_R \hat{e}_x \cdot (\hat{\sigma} \times \vec{k})] \delta(x), \quad (5)$$

where U_0 gives the strength of spin independent potential, while U_R characterize the strength of RSOC. \hat{e}_x is a unit vector directed normal to the interface and $\vec{k} = -i\nabla$.

The fourth term in Eq.(4) represents exchange interaction. The exchange field \vec{h} arises due to the ferromagnetic magnetization for the free layer is described by $\vec{h} = h_0(\sin \theta_m \cos \chi_m, \sin \theta_m \sin \chi_m, \cos \theta_m)$, where θ_m and χ_m respectively are the polar and azimuthal angles of magnetization.

The gap matrix $\hat{\Delta}_{\alpha\beta}(r, r')$ appearing in Eq.(3) has the fol-

lowing form [54]:

$$\hat{\Delta}_{\alpha\beta}(r, r') = \begin{pmatrix} \Delta_{\uparrow\uparrow}(r, r') & \Delta_{\uparrow\downarrow}(r, r') \\ \Delta_{\downarrow\uparrow}(r, r') & \Delta_{\downarrow\downarrow}(r, r') \end{pmatrix} \quad (6)$$

It should be noted that $\Delta_{\uparrow\downarrow}(r, r')$ is a superposition of the singlet (S) and the triplet (T) components that satisfies

$$\Delta_{\uparrow\downarrow}(r, r') = \Delta_{k\uparrow\downarrow}^S(r, r') + \Delta_{k\uparrow\downarrow}^T(r, r'), \quad (7)$$

$$\Delta_{k\uparrow\downarrow}^T(r, r') = \Delta_{k\downarrow\uparrow}^T(r, r'), \quad (8)$$

$$\Delta_{k\uparrow\downarrow}^S(r, r') = -\Delta_{k\downarrow\uparrow}^S(r, r'). \quad (9)$$

Thus, in view of Eqs.(3, 4, 5, 6) the BdG Hamiltonian can be written as

$$\mathcal{H}_{BdG} = \begin{pmatrix} -h_z + H' & g_{k-} - h_{xy} & \Delta_{k\uparrow\uparrow}^T & \Delta_{k\uparrow\downarrow}^S + \Delta_{k\uparrow\downarrow}^T \\ g_{k+} - h_{xy}^* & h_z + H' & -\Delta_{k\uparrow\downarrow}^S + \Delta_{k\uparrow\downarrow}^T & \Delta_{k\downarrow\downarrow}^T \\ \Delta_{k\uparrow\uparrow}^{T\dagger} & -\Delta_{k\uparrow\downarrow}^{S\dagger} + \Delta_{k\uparrow\downarrow}^{T\dagger} & h_z - H' & g_{k+} - h_{xy}^* \\ \Delta_{k\uparrow\downarrow}^{S\dagger} + \Delta_{k\uparrow\downarrow}^{T\dagger} & \Delta_{k\downarrow\downarrow}^{T\dagger} & g_{k-} - h_{xy} & -h_z - H' \end{pmatrix}, \quad (10)$$

where $h_{xy} = h_x - ih_y$, $g_{k\pm} = U_R(k_x \pm ik_y)\Theta(x)$ and $H' = -\frac{\nabla^2}{2} - E_{Fi} + U_0\delta(x)$. $\Theta(x)$ is the Heavyside step function defined by,

$$\Theta(x) = \begin{cases} 0, & x < 0, \\ 1, & x \geq 0. \end{cases} \quad (11)$$

Diagonalizing the Hamiltonian in Eq.(10), we obtain the momenta of electrons and holes in the different regions, which is necessary to calculate the normal and Andreev reflection coefficients, which will be further necessary to calculate the tunneling conductance in a F|NCSC junction. Denoting the momenta for the electrons and the holes in the ferromagnetic region respectively as k^+ and k^- , we get after diagonalizing the BdG Hamiltonian appearing in Eq.(10) as

$$k^\sigma = \sqrt{2(E_{FF} + U_{int} + \vec{h} \cdot \vec{\sigma} \pm E)}, \quad (12)$$

where $\sigma = \pm 1$. In a more explicit way the Eq.(12) can be written as

$$k^\sigma = k_{FF} \sqrt{1 + Z_0 - \sigma Z_R \sin \theta_F - \sigma X \pm Z_1}, \quad (13)$$

where for simplicity we define $Z_0 = \frac{2U_0}{k_{FF}}$, $Z_R = 2U_R$, $X = \frac{M}{E_{FF}}$ and $Z_1 = \frac{E}{E_{FF}}$. Here M is the magnetization of the ferromagnetic region and hence X gives the magnetization strength per unit Fermi energy of the region. Furthermore, the momenta of the electron-like and the hole-like quasiparticles in the superconducting region respectively are denoted by q^+ and q^- , which are found as

$$q^\pm = \sqrt{2(E_{FS} \pm \sqrt{E^2 - \Delta_{\alpha\beta}^2})}. \quad (14)$$

In order to make the calculation easier we set an approximation: $q^+ = q^- = q_{FS}$, where q_{FS} is the Fermi momentum in the superconducting region. The approximation yields an error of the order of $\frac{\delta q_{FS}}{q_{FS}} = \frac{\sqrt{E^2 - \Delta_{\alpha\beta}^2}}{E_{FS}}$, which is of the order of $\frac{\Delta_{\alpha\beta}}{E_{FS}}$ since, $\Delta_{\alpha\beta} \ll E_{FS}$, hence it is a valid approximation.

Again, in the tunneling process the parallel component of momenta is conserved. So we can write,

$$k^+ \sin \theta_F = k^- \sin \theta_A = q^+ \sin \theta_e = q^- \sin \theta_h, \quad (15)$$

where θ_F and θ_A are the angle of incidence of the electron in ferromagnetic region and the retro reflected angle of the hole in the superconducting region respectively. θ_e is the angle of refraction for the electron like quasiparticles, while θ_h is the angle of refraction for the hole like quasiparticles.

Choosing a plane wave solution $\Psi(x) = \psi(x)e^{ikx}$, and introducing it in the Eq.(1) we obtain the wave function for the ferromagnetic region $\Psi_{FM}(x)$ with arbitrary orientation of

magnetization. It can be written as

$$\begin{aligned}
\Psi_{\text{FM}}(x) = & s_{\uparrow} \begin{pmatrix} \cos \theta_m \\ \sin \theta_m e^{-i\chi_m} \\ 0 \\ 0 \end{pmatrix} e^{ik^+ \cos \theta_F x} \\
& + s_{\downarrow} \begin{pmatrix} -\sin \theta_m e^{i\chi_m} \\ \cos \theta_m \\ 0 \\ 0 \end{pmatrix} e^{ik^- \cos \theta_F x} \\
& + r_e^{\uparrow} \begin{pmatrix} \cos \theta_m \\ \sin \theta_m e^{-i\chi_m} \\ 0 \\ 0 \end{pmatrix} e^{-ik^+ S_1 x} \\
& + r_e^{\downarrow} \begin{pmatrix} -\sin \theta_m e^{i\chi_m} \\ \cos \theta_m \\ 0 \\ 0 \end{pmatrix} e^{-ik^+ S_2 x} \\
& + r_h^{\uparrow} \begin{pmatrix} 0 \\ 0 \\ \cos \theta_m \\ \sin \theta_m e^{-i\chi_m} \end{pmatrix} e^{ik^+ S_1 x} \\
& + r_h^{\downarrow} \begin{pmatrix} 0 \\ 0 \\ -\sin \theta_m e^{i\chi_m} \\ \cos \theta_m \end{pmatrix} e^{ik^- S_2 x}, \quad (16)
\end{aligned}$$

where $S_1 = s_{\uparrow} \cos \theta_F + s_{\downarrow} \cos \theta_A$ and $S_2 = s_{\uparrow} \cos \theta_A + s_{\downarrow} \cos \theta_F$. For up spin incident particle we choose $s_{\uparrow} = 1, s_{\downarrow} = 0$, while for a down spin particle $s_{\uparrow} = 0, s_{\downarrow} = 1$. θ_m and χ_m respectively represents the polar angle of magnetization and the azimuthal angle of magnetization as shown in Fig.(1). $r_e^{\uparrow} (r_e^{\downarrow})$ is the normal reflection coefficient for upspin (downspin) electron, while $r_h^{\uparrow} (r_h^{\downarrow})$ is the retro reflection coefficient for the upspin (downspin) hole.

In a similar way for the superconducting layer the wave function can be written [54] as

$$\begin{aligned}
\Psi_{\text{SC}}(x) = & \frac{t_e^{\uparrow}}{\sqrt{2}} \begin{pmatrix} u_+ \\ u_+ e^{-i\phi} \\ -v_+ e^{-i\phi} \\ v_+ \end{pmatrix} e^{iq_e^+ \cos \theta_e x} \\
& + \frac{t_e^{\downarrow}}{\sqrt{2}} \begin{pmatrix} u_- \\ -u_- e^{-i\phi} \\ v_- e^{-i\phi} \\ v_- \end{pmatrix} e^{iq_e^- \cos \theta_e x} \\
& + \frac{t_h^{\uparrow}}{\sqrt{2}} \begin{pmatrix} v_+ \\ v_+ e^{-i\phi} \\ -u_+ e^{-i\phi} \\ u_+ \end{pmatrix} e^{iq_h^+ \cos \theta_h x} \\
& + \frac{t_h^{\downarrow}}{\sqrt{2}} \begin{pmatrix} v_- \\ -v_- e^{-i\phi} \\ u_- e^{-i\phi} \\ u_- \end{pmatrix} e^{iq_h^- \cos \theta_h x}, \quad (17)
\end{aligned}$$

where ϕ is the superconducting phase factor, $t_e^{\uparrow} (t_e^{\downarrow})$ corresponds to the transmission coefficient for up(down) spin Electron-Like Quasiparticles (ELQs), while $t_h^{\uparrow} (t_h^{\downarrow})$ represents the transmission coefficients for up(down) spin Hole-Like Quasiparticles (HLQs). The amplitudes of ELQs and HLQs are given by,

$$u_{\pm} = \frac{1}{\sqrt{2}} \sqrt{1 + \frac{\Omega_{\pm}}{E}}, \quad (18)$$

$$v_{\pm} = \frac{1}{\sqrt{2}} \sqrt{1 - \frac{\Omega_{\pm}}{E}}, \quad (19)$$

with Ω_{\pm} are considered to be as

$$\Omega_{\pm} = \sqrt{E^2 - |\Delta_s \pm \frac{\Delta_t}{2}|^2}. \quad (20)$$

Here, Δ_s and Δ_t are singlet and triplet gap parameters respectively of superconducting states.

The wave functions $\Psi_{\text{FM}}(x)$ and $\Psi_{\text{SC}}(x)$ must satisfy the following boundary conditions:

$$\Psi_{\text{FM}}(x = 0^-) = \Psi_{\text{SC}}(x = 0^+), \quad (21)$$

$$\partial_x [\Psi_{\text{SC}}(x = 0^+) - \Psi_{\text{FM}}(x = 0^-)] = 2U_{\text{int}} \Psi_{\text{FM}}(x = 0). \quad (22)$$

The reflection coefficients ($r_e^{\sigma}, r_h^{\sigma}$) and the transmission coefficients ($t_e^{\sigma}, t_h^{\sigma}$) are calculated using these boundary conditions. Though the explicit expressions for the reflection and the transmission probabilities are too large, however, we have presented an analytic form of the normal and Andreev reflection coefficients for the incidence of an upspin electron in the Appendix.

B. Conductance spectra at the F|NCSC junction

The tunneling conductance of our setup can be calculated by using Blonder - Tinkham - Klapwijk (BTK) formalism [59]. The normalized tunneling conductance $G^{\sigma}(E, \theta_F)$ for an incoming electron of spin σ with an incident angle θ_F at the junction reads as

$$G^{\sigma}(E, \theta_F) = G_N^{-1} \left[1 + \sum_{\sigma} (|r_h^{\sigma}(E, \theta_F)|^2 - |r_e^{\sigma}(E, \theta_F)|^2) \right], \quad (23)$$

where G_N is the tunneling conductance for N|N (Normal metal-Normal metal) junction for an interface potential U_0 and has the following form:

$$G_N = \int_{-\frac{\pi}{2}}^{\frac{\pi}{2}} d\theta_F \frac{4 \cos^3 \theta_F}{4 \cos^2 \theta_F + Z_0^2}. \quad (24)$$

Thus, in view of this the angularly averaged conductance can be written as [46, 52, 54, 59, 60]

$$G(E) = G_N^{-1} \int_{-\frac{\pi}{2}}^{\frac{\pi}{2}} d\theta_F \cos \theta_F P^{\sigma} G^{\sigma}(E, \theta_F), \quad (25)$$

where P^σ is the spin dependent probability factor for the spin injection σ and can be read as [46]

$$P^\sigma = \frac{(1 + \sigma X)}{2}. \quad (26)$$

In this work, we have plotted the angularly averaged normalized conductance $G(E)$ that appears in (25) as a function of biasing energy E scaled by the gap amplitude parameter $|\Delta_\pm|$, where $|\Delta_\pm| = |\Delta_s \pm \frac{\Delta_t}{2}|$. From the earlier works [46–48], it is seen that the conductance has a strong dependence on singlet-triplet gap magnitudes. In all our analysis, we considered $\Delta_s = \frac{\Delta_t}{3}$. However, to understand its effect on conductance characteristics, we have also investigated the conductance spectrum for different singlet-triplet mixing magnitudes too, since in NCSC the gap magnitude played a very important role. It is well known from the previously mentioned experimental works that the NCSC possess a strong ASOC [29–35] due to the lack of inversion center. Recently, with the increased applications of spintronics in last few years, the phenomenon of SOC gains a lot of attention. So, the central point of our work is to study the effect of RSOC on the tunneling conductance spectrum.

Though magnetization plays a very important role in ferromagnetic superconductors, but its interplay with RSOC and hence on the conductance spectrum characteristics in F|NCSC junction of a F|S|F spin valve is still need to be understood. So we also investigated the role of magnetization strength (X), polar (θ_m) and the azimuthal angles of magnetization (χ_m) on the tunneling conductance. Moreover, we have also investigated its effect on the RSOC. To understand the orientation dependence of the conductance characteristics, we have plotted the Zero Bias Conductance (ZBC) with polar angle of magnetization for different azimuthal angles of magnetization, different magnetization strength and also for different RSOC. Moreover, the dependence of ZBC on the azimuthal angles of magnetization is also studied for different magnetization strengths, polar angles of magnetization as well as for different RSOC's.

It should be noted here that there exist a strong dependence of the conductance characteristics on the barrier transparency. So we also investigated the effect of barrier transparency on conductance spectrum, RSOC as well as on magnetization. Usually, in Andreev reflection experiments of an F|NCSC junction, the Fermi momentum in the different regions are different. It arises due to unequal densities of the local charge carries in different regions. In this regard, the effect of FWM on conductance characteristics of an F|NCSC junction and how it will competes with magnetization and RSOC need to be understood properly, and hence we have considered a dimensionless parameter λ , which measures the ratio of Fermi wave-vectors in different layers as mentioned earlier. In this work, we consider the value of λ as 0.5, 1.0, 1.25 and 1.5. For all our analysis we consider Z_1 to be very small and we assume $Z_1 = 0.001$.

III. RESULTS AND DISCUSSIONS

A. Effect of Rashba spin orbit coupling (RSOC)

To understand the effect of RSOC on the tunneling conductance, we have plotted the normalized conductance $G(E)$ with biasing energy in Fig.(2) for three different choices of RSOC strength, viz., $Z_R = 0, 0.5$ and 1.5 considering a nearly transparent barrier ($Z_0 = 0.1$). We consider the singlet-triplet gap amplitudes as $\Delta_s = \frac{\Delta_t}{3}$ for our analysis. The figures in the top panel are plotted for a magnetization strength $X = 0.8$ while for the figures in the bottom panel we consider $X = 1.0$. The mismatch parameter λ is considered to be as 1.5 for our analysis in Fig.(2). For the figures in the top panel we have considered the polar angle θ_m as $0, 0.25\pi$ and 0.5π keeping the azimuthal angle $\chi_m = 0$ in the first two plots of top panel of Fig.(2). The figure on the right of top panel is drawn for $\theta_m = 0.5\pi$ and $\chi_m = 0.25\pi$.

Due to the formation of Andreev bound states near $E = \Delta_- = |\Delta_s - \frac{\Delta_t}{2}|$ and at $\Delta_+ = |\Delta_s + \frac{\Delta_t}{2}|$, two sharp peaks in the conductance spectra are observed. The conductance is found to be maximum for Rashba free case, while it is significantly decreased in presence of RSOC as seen from all the plots of Fig.(2). It is maximum for the low energy regions i.e. $E < \Delta_-$, then it gradually decreases for low Rashba cases i.e. for $Z_R = 0$ and 0.5 while for $Z_R = 1$, no significant change is seen. It shows a peak near Δ_- for $\theta_m = 0.25\pi$, $\chi_m = 0$ and $X = 0.8$ in all RSOC's. For the region $\Delta_- < E < \Delta_+$, in every cases it decreases rapidly and then rises monotonically till Δ_+ . For all the plots a sharp peak it observed at $E = \Delta_+$. A similar characteristics is also seen for $X = 1.0$. However, in this case the decrease in conductance is quite gradual. For $\theta_m = 0.25\pi$, $\chi_m = 0.5\pi$ and $X = 1.0$, the conductance shows two very sharp peaks near $0.17\Delta_t$ and $0.83\Delta_t$ as shown in middle plot of bottom panel of Fig.(2). A similar characteristics is also observed for $X = 0.8$ as seen from the left plot of Fig.(3). The peak near $0.17\Delta_t$ nearly disappeared for $\theta_m = 0.5\pi$. In Fig.(3), we consider the effect of barrier strength Z_0 . For this purpose, we consider $\theta_m = 0.25\pi$, $\chi_m = 0.5\pi$, $X = 0.8$ and $\lambda = 1.5$. We studied the conductance characteristics for a transparent ($Z_0 = 0$), partially opaque ($Z_0 = 2$) and a strongly opaque ($Z_0 = 5$) barriers in Fig.(3). The conductance has been analyzed for Rashba free case ($Z_R = 0$), weak RSOC ($Z_R = 0.5$), and for moderate RSOC ($Z_R = 1$). Though the conductance gets decreased with the rise of RSOC as seen earlier, however a reverse trend is seen for $Z_0 = 2$. In this case, it is found that the conductance gradually increases with the rise of RSOC. Another important point is that there is a suppression of broadening of the peak which is quite significant for $Z_0 = 0$. For a strongly opaque barrier ($Z_0 = 5$), the effect of RSOC is not too significant as seen from the right plot of Fig(3). So, what is the role of barrier strength on RSOC and how it effects the maximum conductance?

In order to understand that it is necessary to investigate the variation of maximum normalized conductance G_{max} with the RSOC (Z_R) for different barrier transparency (Z_0). We have plotted the same in Fig.(4) for $Z_0 = 0, 2$ and 5 . The plot

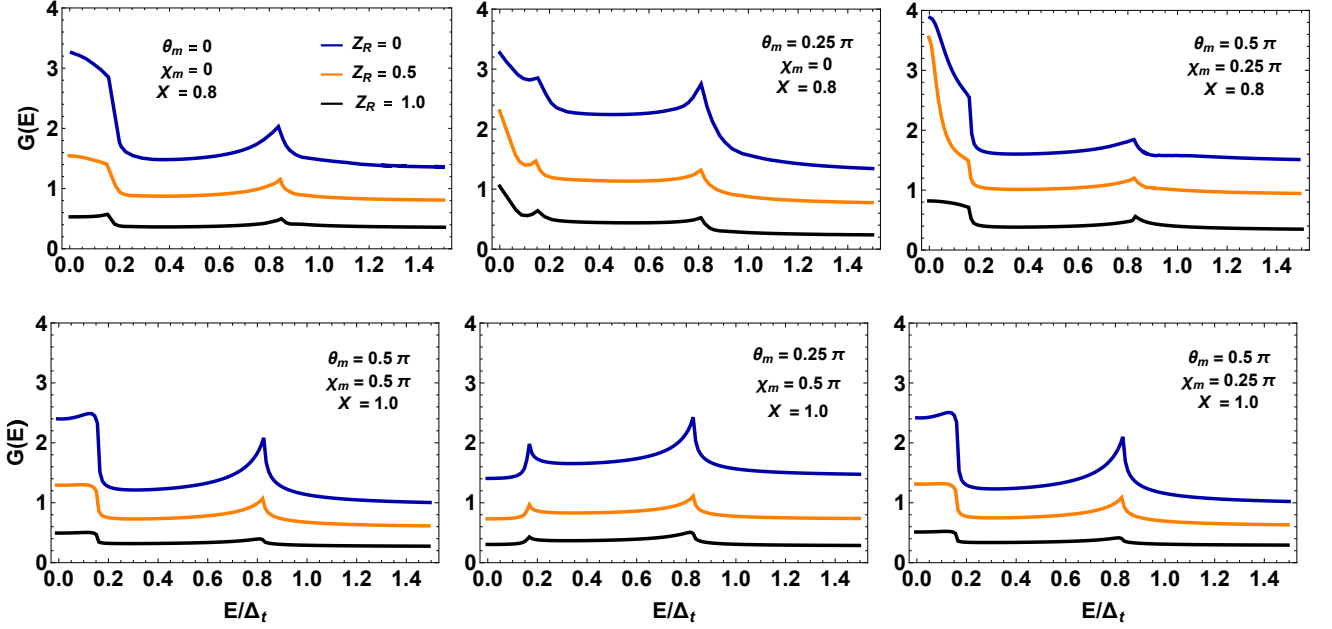


FIG. 2: Conductance spectra for different values of Z_R with $\Delta_s = \frac{\Delta_t}{3}$, $Z_0 = 0.1$, $\lambda = 1.5$. The figures in the top panel is for $X = 0.8$, while the bottom panel is for $X = 1.0$ for different orientations of magnetization.

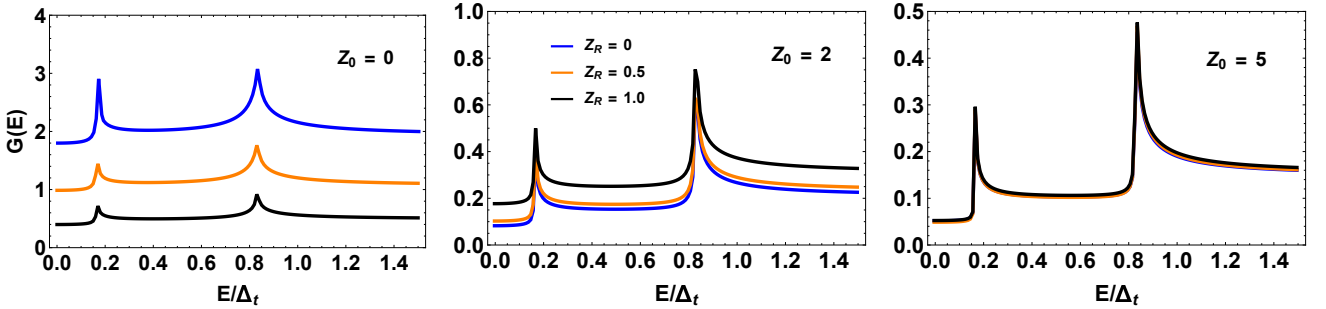


FIG. 3: Dependence of conductance $G(E)$ on the barrier transparency Z_0 for $\theta_m = 0.25\pi$, $\chi_m = 0.5\pi$ and $X = 0.8$ with $\lambda = 1.5$.

in the left is for $\lambda = 0.5$, while the right for $\lambda = 1.5$. It is seen that for a transparent barrier the maximum conductance G_{max} shows a sharp peak near $Z_R \simeq 0.1$ and a gradual decrease is seen with the further increase in Z_R . Similar characteristics are also observed for an opaque barrier. For $Z_0 = 2$, a sharp peak is seen at $Z_R \simeq 2$, which sharply decrease with the further rise of Z_R as seen earlier for a transparent barrier. However, for $Z_0 = 5$, it shows nearly a linear behaviour for low values of RSOC while rises sharply for higher values of Z_R . An exactly similar characteristics of G_{max} is also observed for $\lambda = 1.5$. It is also observed that with the increase in FWM parameter λ , G_{max} also increases.

We studied the effect of FWM on the conductance spectrum, which is shown in Fig.(5). For this purpose, we investigated the conductance spectra for three different choices of λ , viz., (i) for $q_{FS} < k_{FF}$ with $\lambda = 0.5$ (left plot), (ii) no mismatch $q_{FS} = k_{FF}$ with $\lambda = 1.0$ (middle plot), and (iii) for $q_{FS} > k_{FF}$ with $\lambda = 1.25$ (right plot). We consider, $\theta_m = 0.25\pi$, $\chi_m = 0.5\pi$, $X = 0.8$ and a transparent barrier

with $Z_0 = 0$ for this analysis. It is seen that the characteristics of the conductance spectrum is independent of λ . However, rise of FWM parameter λ enhances the conductance for all values of RSOC as seen from Fig.(5).

1. Dependence of Zero Bias Conductance (ZBC) on the polar angle of magnetization θ_m

It should be noted that there exist a peak even at $\theta_m = 0$ and there exist a significant change with the polar angle of magnetization and magnetization strength as seen from Fig.(2). Though there is a very small variation in conductance with the azimuthal angle, however its effect cannot be neglected. To understand the magnetization orientation dependence of conductance spectrum we have plotted the ZBC as a function of θ_m with different choices of χ_m , X and λ in Fig.(6). All the plots are drawn for a nearly transparent barrier ($Z_0 = 0.1$) and for different RSOC coupling strengths

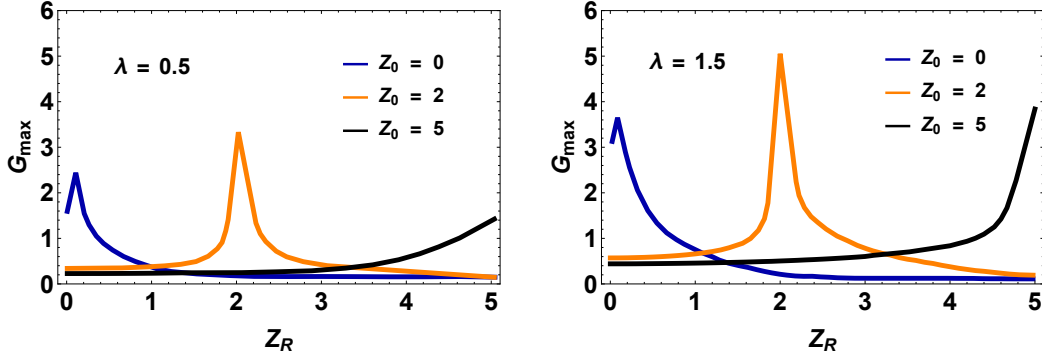


FIG. 4: Variation of G_{\max} with RSOC parameter Z_R for different barrier strengths $Z_0 = 0, 2$ and 5 respectively. The plot in the left is for $\lambda = 0.5$, while the plot in the right is for $\lambda = 1.5$.

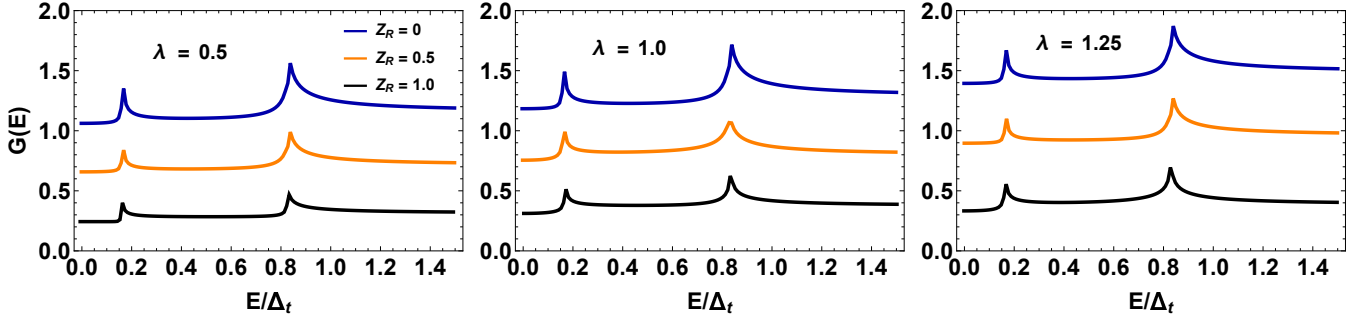


FIG. 5: Conductance spectra for different FWM parameter λ with magnetization strength $X = 0.8$, polar angle of magnetization $\theta_m = 0.25\pi$, azimuthal angle of magnetization $\chi_m = 0.5\pi$ and barrier strength $Z_0 = 0$. The three different lines in the plots represent different choices of RSOC (Z_R).

Z_R . Though the effect of azimuthal angle is still need to be known, however for $\chi_m = 0$, the ZBC remains constant for all the choices of X and λ . It is observed from all the plots that the ZBC plots are highly symmetrical about θ_m for non vanishing χ_m . For $\chi_m = 0.25\pi$, $X = 0.8$ and $\lambda = 1.5$, it shows an oscillatory behaviour having a ZBC Peak (ZBCP) at $\theta_m = 0, 0.5\pi$ and at π for all the RSOC's as seen from the left top plot of Fig.(6). Usually the ZBCP appears in unconventional superconductors due to the different phases of the transmitted electronlike and holelike quasi particles in the superconducting region [53]. However, according to Zutic and Valls [49, 50], the appearance of ZBCP is due to the FWM and it may also appear in conventional superconductors too. With the increase of X to 1.0, a significant change in the ZBC spectrum is observed for $Z_R = 0$. The ZBC characteristics remains quite similar as for $Z_R = 0.5$ and 1.0 as seen from the plot in the left bottom of Fig.(6). In both cases the only significant observation is that with the rise of magnetization strength, the ZBC drastically decreases with the increasing values of Z_R . The plots in the middle panel (vertical) are drawn for the FWM $\lambda = 1.25$ and for two different choices of magnetization strength respectively 0.8 and 1.0. For $\lambda = 1.25$ with $X = 0.8$, the conductance characteristics is exactly similar with $\lambda = 1.5$ for $Z_R = 0.5$ and 1.0. The conductance characteristics shows a significant change for Rashba free case for $\lambda = 1.25$. In this condition the oscillatory characteristics

nearly vanishes, it gradually falls from a maxima and then remains constant followed by a small peak at $\theta_m = 0.5\pi$ as seen from the middle plot of the top panel of Fig(6). Another important result we have seen that with the increase of FWM, the conductance increases by a significant amount. A totally opposite behaviour from $X = 0.8$ is observed for $X = 1.0$ with $\lambda = 1.25$. In this case, ZBC Dips (ZBCDs) are observed at $\theta_m = 0, 0.5\pi$ and π , from which the ZBC gradually rises, saturates and falls to the next dip as seen from the middle plot of the bottom panel of Fig(6). It is to be noted that for non vanishing values of RSOC's, the ZBC characteristics are almost similar. So it can be concluded that the ZBC spectrum highly dependent on FWM parameter and the strength of magnetization. We have also investigated the ZBC for $\chi_m = 0.5\pi$, $X = 1.0$ and $\lambda = 1.5$. In this condition a very small change in the behaviour of ZBC is observed for Rashba free case as obtained for $\chi_m = 0.25\pi$ (see bottom left plot), however no significant change is observed with the rise of RSOC. So it can also be concluded that the ZBC spectrum is nearly independent for higher values of RSOC strength.

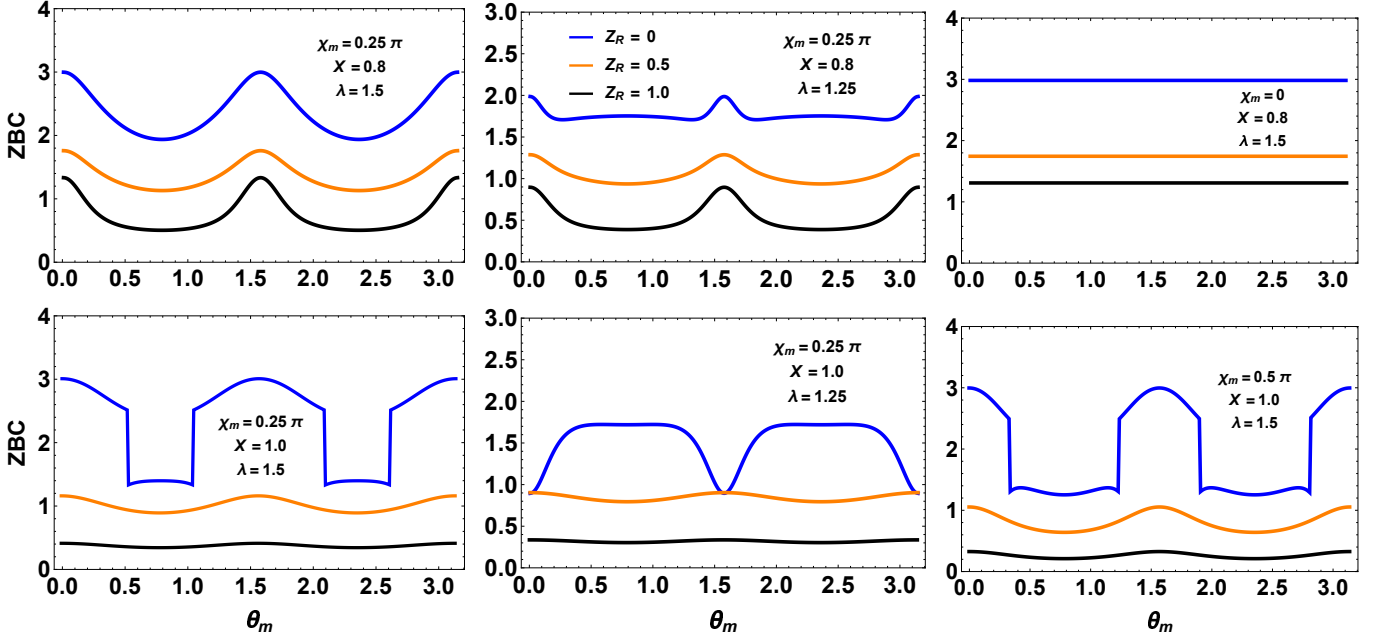


FIG. 6: Variation of ZBC with polar angle of magnetization (θ_m) for different magnetization strength X , azimuthal angle of magnetization χ_m . The FWM are considered to be as $\lambda = 1.25$ and 1.5 respectively. The plot in the top left panel is for $X = 0.8$, while the bottom left plot is for $X = 1.0$ with $\lambda = 1.5$. The middle line plots are drawn for $\lambda = 1.25$. The plot in the top right panel is for $\chi_m = 0$ and $X = 0.8$, while in the bottom right plot we consider $\chi_m = 0.5\pi$ and $X = 1.0$ keeping $\lambda = 1.5$ fixed.

2. Dependence of ZBC on the azimuthal angle of magnetization χ_m

The variation of ZBC with the azimuthal angle is shown in Fig.(7) for different FWM and the magnetization strength considering a transparent barrier i.e. $Z_0 = 0.1$. We consider the polar angle of magnetization as $\theta_m = 0.25\pi$ for our analysis. However, we have also analyzed the ZBC characteristics for $\theta_m = 0$ and 0.5π as shown in the top and bottom of the right plots of the figure respectively. It is seen that the ZBC behaviour is totally opposite for $\lambda = 1.25$ as observed from 1.5. For $\lambda = 1.5$ a valley like pattern is seen while for $\lambda = 1.25$ a hill like characteristics is observed for Rashba free case. In the first case for $\lambda = 1.5$, the ZBC spectra has a minima at $\chi_m = 1.5\pi$, while for the preceding i.e. for $\lambda = 1.25$ it has a maxima at $\chi_m = 1.5\pi$ as seen from the middle top plot of Fig.(7). It is to be noted that there is no significant change in ZBC with the change in the mismatch parameter λ in presence of RSOC. The only observed change is with the rise in mismatch parameter λ the conductance increases for all the values of RSOC as seen from the plots of Fig.(7). It is also observed that for the polar angle $\theta_m = 0$ and 0.5π , there exist no change in the ZBC characteristics. So it can be concluded from here that ZBC spectra is highly dependent on orientation of the polar angle too for Rashba free cases. For experimentally suitable conductance, arbitrary orientation of the polar angle is preferred. Furthermore, it can be concluded that with the rise of RSOC, the orientation dependence of ZBC is lost.

3. Dependence of ZBC on the strength of magnetization X

To understand the interplay of magnetization with RSOC and their role on conductance characteristics, we studied the variation of ZBC spectra with the magnetization strength (X) in Fig.(8). For this purpose we choose three different types of barriers mentioned in the earlier occasions, viz., $Z_0 = 0, 2$ and 5 respectively for a highly transparent, partially opaque and fully opaque barriers. Moreover, for this analysis we choose $\theta_m = 0.25\pi$, $\chi_m = 0.5\pi$ and $\lambda = 1.5$. It is seen that for a highly transparent barrier the ZBC spectra shows a gradual rise with the rise in X . A ZBCP is observed at $X \approx 0.7$ for all Rashba cases. However, further rise of magnetization strength leads to decrease in the conductance as seen from the left plot of Fig.(8). The ZBC characteristics drastically changes for a partially opaque and a strongly opaque barrier. In both the cases it is seen that the conductance decreases almost linearly with the rise of strength of the magnetization for all Rashba cases as seen from the middle and the right plots of the figure. Another significant result is that for a partially opaque and fully opaque barrier i.e. $Z_0 = 2$ and 5 all Rashba cases provide maximum conductance at $X \approx 0$. The characteristics of the ZBC spectra are found to be nearly similar for all Rashba cases for opaque barriers. It is observed that for a transparent barrier, Rashba free cases provide the maximum conductance and it decreases with the increasing values of RSOC, while for a partially opaque barrier an opposite behaviour is observed. In this case with the rise of RSOC, the conductance increases. It is to be noted that for a strongly opaque barrier i.e. $Z_0 = 5$,

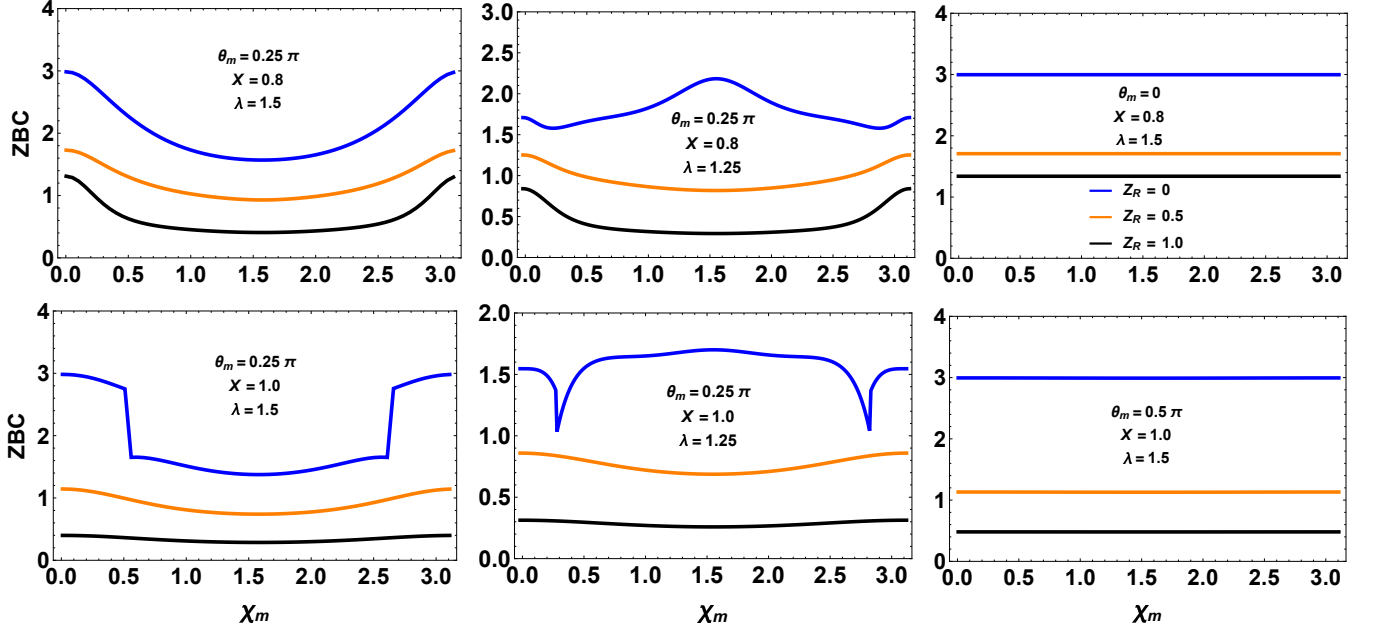


FIG. 7: Variation of ZBC with azimuthal angle of magnetization χ_m for different magnetization strength X and polar angle of magnetization θ_m . The FWM are considered to be as $\lambda = 1.25$ and 1.5 respectively. The plot in the top left panel is for $X = 0.8$, while the bottom left panel plot is for $X = 1.0$ keeping $\lambda = 1.5$ fixed. The middle line plots are drawn for $\lambda = 1.25$. The plot in the top right panel is for $\theta_m = 0$ and $X = 0.8$, while in the bottom of right plot we consider $\theta_m = 0.5\pi$ and $X = 1.0$ keeping $\lambda = 1.5$ fixed.

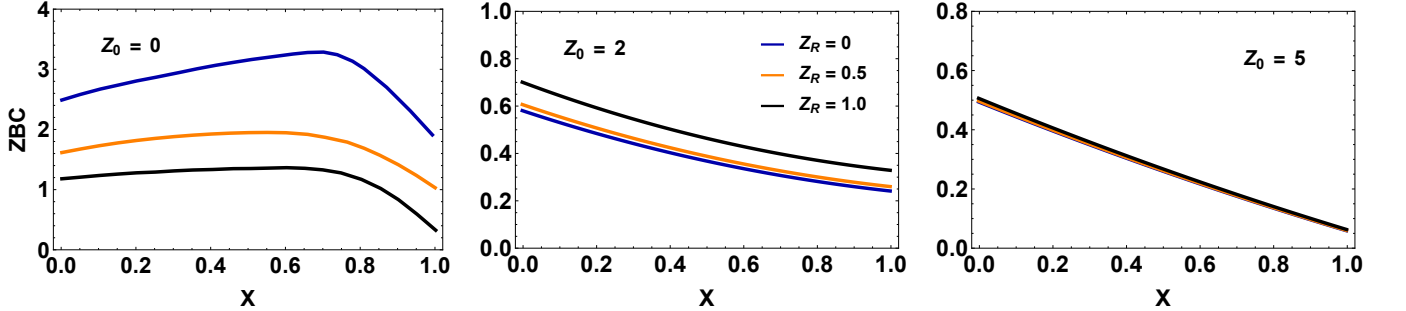


FIG. 8: Dependence of ZBC on the magnetization strength X for different barrier strengths Z_0 . The figures are plotted for $\lambda = 1.5$, $\theta_m = 0.25\pi$, $\chi_m = 0.5\pi$. The figure in the left is for $Z_0 = 0$, middle figure is for $Z_0 = 2$, while the figure in the right is for $Z_0 = 5$.

the effect of RSOC on the ZBC is almost insignificant. So, it can be concluded here that a highly transparent barrier with moderate RSOC along with moderate magnetization strength is highly suitable for an experimentally realistic scenario.

B. Effect of Magnetization

It is clear from Figs.(6), (7) and (8) of the preceding section that the ZBC spectra is highly dependent on magnetization. It is seen that conductance not only depend on the strength of magnetization but also dependent on the orientation of magnetization. To understand the role of magnetization more clearly and its interplay with RSOC, we have plotted the conductance $G(E)$ as appear in the Eq.(25) with the biasing energy E scaled by the gap parameter Δ_{\pm} for different choices of the

strength of magnetization X . For this purpose, we initially consider a highly transparent barrier i.e. $Z_0 = 0$. We have also investigated the same for a partially opaque barrier i.e. $Z_0 = 1$. We vary the polar angle of magnetization θ_m keeping the azimuthal angle χ_m and the strength of magnetization X fixed. The results are shown in the plots appear on the top panel of Fig.(9). We have also analyzed the conductance characteristics by varying azimuthal angle of magnetization χ_m keeping the polar angle θ_m and the strength of magnetization X fixed. This results are shown in plots on the top panel of Fig.(10). The plots on the bottom panel of Figs.(9) and (10) represent the conductance spectra for different strength of X keeping χ_m and θ_m constant respectively.

To understand the significance of the azimuthal angle χ_m we plotted the conductance spectra considering $Z_0 = 0$, $Z_R = 1$ and $X = 0.7$ for $\chi_m = 0.1\pi$ (middle of bottom

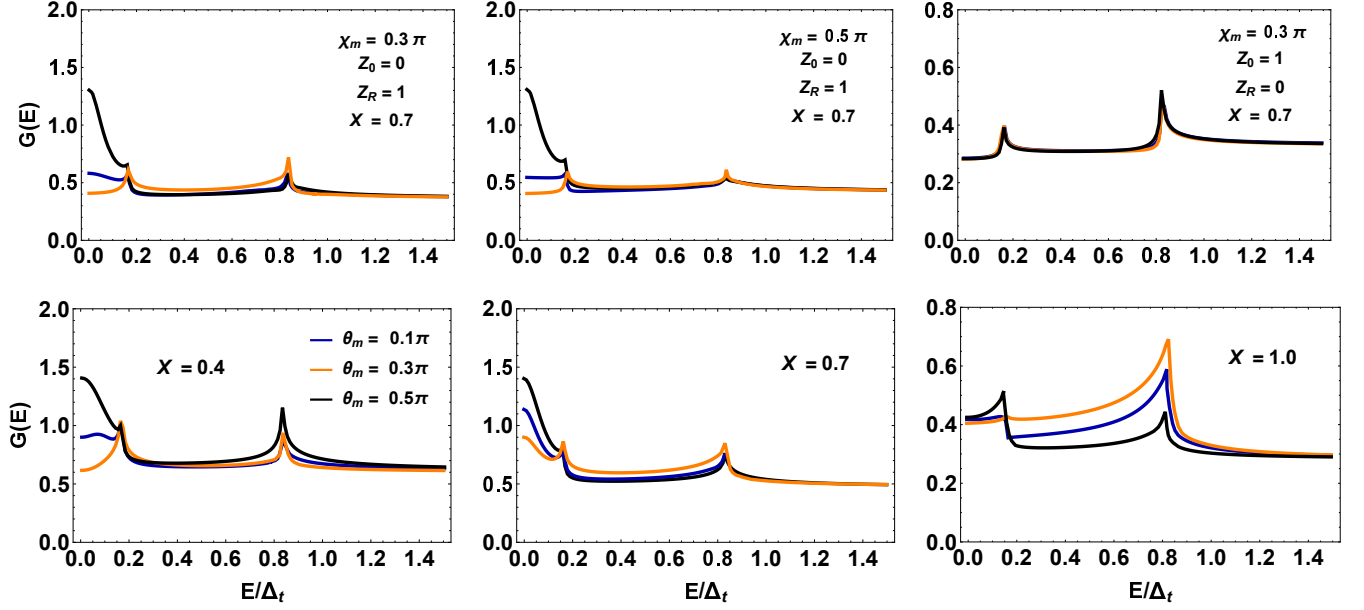


FIG. 9: Conductance spectra for different the azimuthal angle of magnetization χ_m and the strength of magnetization X . The left and the middle figures in the top panel are plotted respectively for $\chi_m = 0.3\pi$ and 0.5π with $Z_0 = 0$ and $Z_R = 1$. The figure in the top right is plotted for $\chi_m = 0.3\pi$, $Z_0 = 1$ and $Z_R = 0$. The bottom figure in the left is for $X = 0.4$, middle is for $X = 0.7$ and the right is for $X = 1.0$. For the bottom figures we choose $\chi_m = 0.1\pi$, $Z_0 = 0$ and $Z_R = 1$.

panel), $\chi_m = 0.3\pi$ (left of top panel) and $\chi_m = 0.5\pi$ (middle of top panel) in Fig.(9). For all our analysis here we consider FWM $\lambda = 1.5$. It is seen that the pattern of conductance spectrum is quite similar for all studied orientations of χ_m . The conductance is found to be maximum for $\chi_m = 0.1\pi$ with $X = 0.7$. In this case a sharp peak is observed as E approaches to Δ_- and Δ_+ similar to the spectra seen earlier for different RSOC's. Another important point is that the conductance characteristics is nearly similar for arbitrary ($\theta_m = 0.3\pi$) and perpendicular orientations ($\theta_m = 0.5\pi$) of the polar angle of magnetization θ_m with $\chi_m = 0.5\pi$ and $X = 0.7$. For perpendicular orientation of θ_m , the sharpness of the conductance peak is found to be minimum as seen from the plot on the middle of top panel. we are also interested to see the behaviour of conductance spectrum for a partially opaque barrier with $Z_0 = 1$. It is observed that for an opaque barrier the conductance spectrum is totally independent on the strength as well as the orientation of polar angle of magnetization as seen from the plot at the right of the top panel of Fig.(9). We have also studied the conductance spectra for three different choices of magnetization strength, viz., $X = 0.4$ (left of bottom panel), $X = 0.7$ (middle of bottom panel) and $X = 1.0$ (right of bottom panel) with $\chi_m = 0.1\pi$, $Z_0 = 0$ and $Z_R = 1$. It is to be noted here that for $M \ll E_F$, the conductance is found to be maximum for $\theta_m = 0.5\pi$, while it is found to be minimum as $M \rightarrow E_F$. In this situation, the arbitrary configuration of θ_m shows maximum conductance as seen from the plots of middle and right of the bottom panel of Fig.(9). It is also observed that the conductance spectrum gets suppressed with the rise of magnetization

strength.

It is also our interest to see the interplay of polar angle of magnetization θ_m with conductance. Thus we studied the conductance spectra considering $Z_0 = 0$, $Z_R = 1$ and $X = 0.7$ for $\theta_m = 0.1\pi$ (middle of bottom panel), $\theta_m = 0.3\pi$ (left of top panel) and $\theta_m = 0.5\pi$ (middle of top panel) as shown in Fig.(10). It is seen that for perpendicular orientation of polar angle of magnetization, the conductance spectra are totally independent on the orientation of azimuthal angle χ_m of magnetization. Though the two peaks appear in all three situations but the sharpness of the peak is very small in this condition. For $\theta_m = 0.1\pi$ and 0.3π , the conductance is found to be maximum for $\chi_m = 0.1\pi$, while it is minimum for $\chi_m = 0.5\pi$ as seen from the plots of Fig.(10) as mentioned above. It is also noted that with the decrease in the transparency of the barrier with $Z_0 = 1$, the conductance characteristics is almost independent on the orientation of azimuthal angle of magnetization as seen from the plot on top right panel of Fig.(10) as seen earlier in Fig.(9). We have also studied the conductance spectra for three different choices of magnetization strength viz., $X = 0.4$ (left of bottom panel), $X = 0.7$ (middle of bottom panel) and $X = 1.0$ (right of bottom panel) with $\theta_m = 0.1\pi$, $Z_0 = 0$ and $Z_R = 1$. Another important point is for $M \ll E_F$, the conductance is found to be maximum for $\chi_m = 0.5\pi$, while it is found to be minimum as $M \rightarrow E_F$ as in the case for $\theta_m = 0.5\pi$. In this situation, the orientation $\chi_m = 0.1\pi$ shows maximum conductance as shown in the plots of middle and right of the bottom panel of Fig.(10).

We are also interested to see the variation of ZBC spectra for different strength of magnetization and the barrier trans-

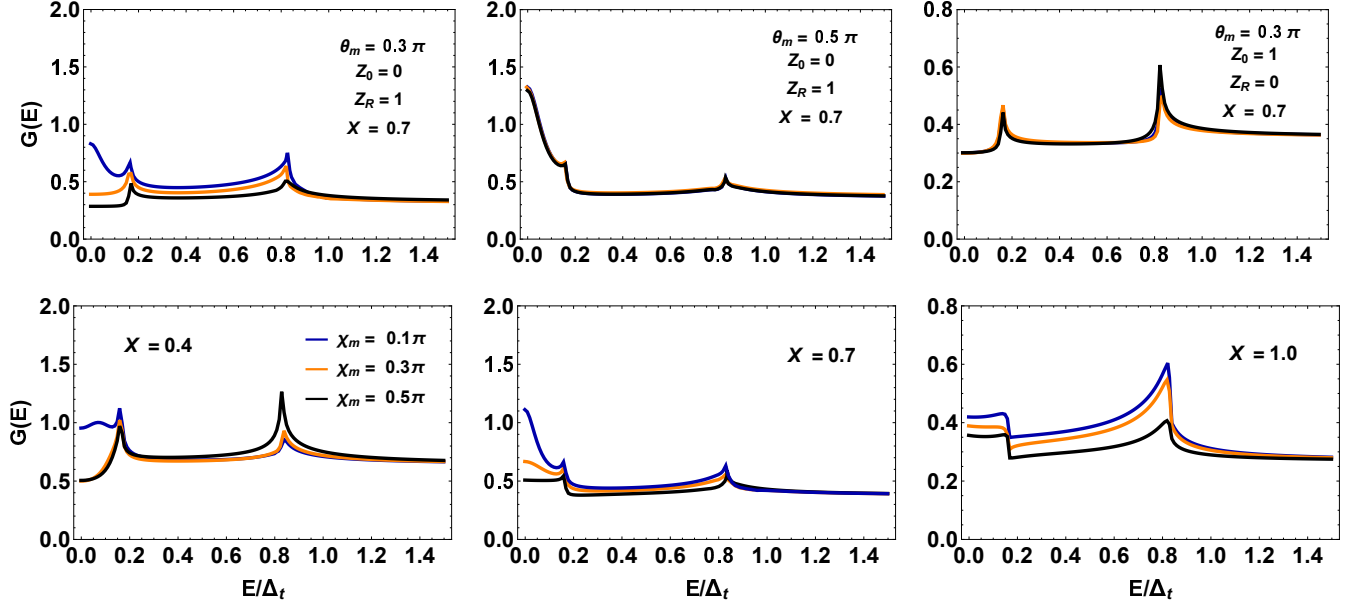


FIG. 10: Conductance spectra for different the polar angle of magnetization θ_m and the strength of magnetization X . The left and the middle figures in the top panel are plotted respectively for $\theta_m = 0.3\pi$ and 0.5π with $Z_0 = 0$ and $Z_R = 1$. The figure in the top right is plotted for $\theta_m = 0.3\pi$, $Z_0 = 1$ and $Z_R = 0$. The bottom figure in the left is for $X = 0.4$, middle is for $X = 0.7$ and the right is for $X = 1.0$. For the bottom figures we choose $\theta_m = 0.1\pi$, $Z_0 = 0$ and $Z_R = 1$

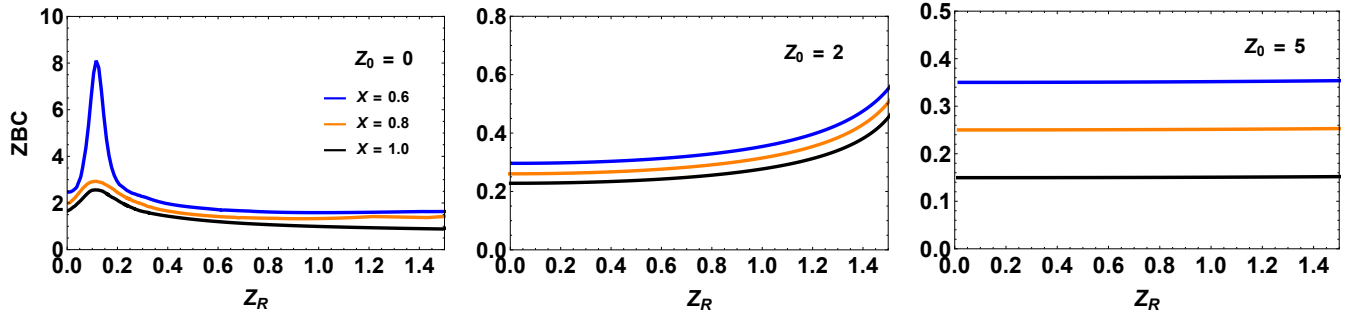


FIG. 11: Dependence of ZBC on the RSOC (Z_R) for different barrier strengths Z_0 . The figures are plotted for $\lambda = 1.5$, $\theta_m = 0.5\pi$, $\chi_m = 0.5\pi$. The figure in the left is for $Z_0 = 0$, middle figure is for $Z_0 = 2$, while the figure in the right is for $Z_0 = 5$.

parency. For this purpose we studied the variation of ZBC spectra with RSOC parameter Z_R for a transparent barrier ($Z_0 = 0$), partially opaque barrier ($Z_0 = 2$) and a strongly opaque barrier ($Z_0 = 5$), which is shown in Fig.(11). In all the cases, it is seen that with the rise in the strength of magnetization X the ZBC decreases. Also, with the decrease in transparency of the barrier the conductance decreases. The ZBC is found to be maximum for $X = 0.6$, while it decreases as $M \rightarrow E_F$. A sharp ZBCP is seen for transparent barrier nearly at $Z_R = 0.1$ for all choices of X . However, the sharpness of the peak is found to be maximum for $X = 0.6$. With the increase in RSOC, the ZBC decreases monotonically for $Z_0 = 0$. A similar characteristics in ZBC spectra is also seen for a partially opaque barrier with $Z_0 = 2$. However, in this case the ZBC increases with Z_R and hence the ZBCP

appears for the higher values of Z_R as seen from the middle plot of Fig.(11). So, it can be concluded that the with the decrease in transparency of the barrier the ZBCP appear for higher values of RSOC. For a strongly opaque barrier ZBC characteristics is found to be totally independent of RSOC.

C. Effect of different singlet-triplet mixing ratio

It is of our interest to see what happens to the conductance for different spin singlet-triplet mixing. Also it was found that a highly transparent barrier is often realizable from many Scanning Tunneling Microscope (STM) experiments [54, 55]. So in view of the experimentally suitable situation we studied the conductance spectrum of a highly transparent barrier with

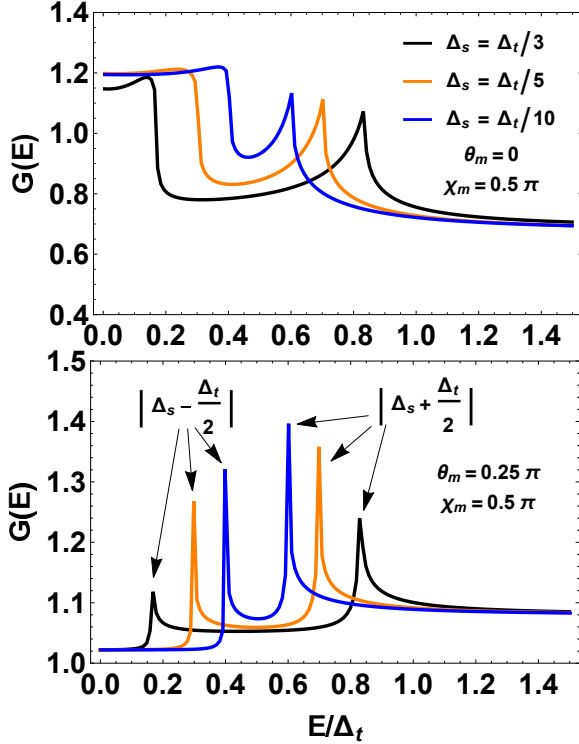


FIG. 12: Conductance spectra for different mixing of singlet-triplet gap parameter with magnetization strength $X = 1.0$, azimuthal angle of magnetization $\chi_m = 0.5\pi$, RSOC parameter $Z_R = 0.5$ and barrier strength $Z_0 = 0$. The plot in the top panel is for polar angle $\theta_m = 0$, while the plot in the bottom panel is for $\theta_m = 0.25\pi$. The three different lines represent different choices of Δ_s .

$Z_0 = 0$ for three different spin singlet-triplet mixing as shown in Fig.(12). We consider the RSOC parameter $Z_R = 0.5$, FWM parameter $\lambda = 1.5$, azimuthal angle of magnetization $\chi_m = 0.5\pi$ and the strength of magnetization $X = 1.0$ for this analysis. For the figure on the top we consider the polar angle of magnetization $\theta_m = 0$, while for the bottom figure it is 0.5π . It is seen that with the increase in the ratio of $\Delta_t : \Delta_s$, the appearance of the conductance peaks at Δ_- and Δ_+ is quite nearer each other. It is also to be noted that with the increase in the ratio of $\Delta_t : \Delta_s$, the sharpness of the conductance peaks gradually increases as seen from both the plots of Fig.(12). So it can be concluded that from the sharpness of conductance spectra, the relative size of mixing of spin singlet and triplet components of the gap parameter can be inferred. Our result is highly in accordance with the results of Ref. [54].

IV. SUMMARY AND CONCLUSIONS

In summary, in this paper we have investigated the conductance spectra at the interface of F|NCSC of a F|S|F spin valve using an extended Blonder - Tinkham - Klapwijk (BTK) approach and the scattering matrix formalism. We developed

the Bogoliubov de Gennes (BdG) Hamiltonian for such a hybrid structure introducing the RSOC and the arbitrary orientation of the magnetization. We have demonstrated conductance spectra for an experimentally realistic parameter set, which suggest a high transparency and a moderate RSOC. Though low value of FWM is generally preferred, however we have considered both low and high values of FWM for our analysis. Many conclusions can be drawn from our analysis. It is seen that the conductance spectra is orientation dependent. The barrier transparency and RSOC play a very significant role. RSOC in general suppresses the conductance for a transparent barrier with any arbitrary orientation of the magnetization, however for a partially opaque barrier it monotonically rises with the increase of RSOC. The conductance becomes maximum for mid values of RSOC and then gradually fall for higher values of RSOC. For a strongly opaque barrier the conductance spectrum is found to be nearly independent of RSOC. Moreover, it is observed that the strength of magnetization and its orientations also plays a very important role in the conductance spectrum. The charge conductance characteristics is found to be as orientation dependent. The presence unconventional superconductor and for different FWM, a zero bias conductance peak (ZBCP) and dip (ZBCD) is observed. Another important point is that for a barrier with high transparency, the rise of strength of magnetization enhances the conductance, however Andreev reflection decreases which shows a decrease in conductance as magnetization approaches the Fermi energy. For an opaque barrier the rise of strength of magnetization suppresses the charge conductance. It is also observed that with the rise of singlet-triplet mixing ratio the conductance decreases.

As a concluding remark, the results of our work indicates that a highly transparent spin active barrier with moderate RSOC and moderate strength of magnetization having an arbitrary orientation is highly suitable for a practical nano spin valve involving a noncentrosymmetric superconductor. We sincerely hope that our results shed some light on ferromagnet and noncentrosymmetric superconductor hybrid structures which can be utilized to make practical superconducting spintronic devices in near future.

Appendix A: Calculation of reflection and transmission coefficients

Using BTK formalism and boundary conditions (21) and (22) in the wavefunctions $\Psi_{FM}(x)$ and $\Psi_{SC}(x)$ given in Eqs.(16) and (17) respectively, we obtain 8 linear equations connecting the reflection and transmission coefficients. The analytic expressions for reflection and the transmission coefficients can be obtained by solving the equation of the form $x = \mathcal{A}^{-1}\mathcal{B}$, where \mathcal{A} is a 8×8 matrix, while \mathcal{B} is 8×1 matrix and $x = (r_e^\uparrow, r_e^\downarrow, r_h^\uparrow, r_h^\downarrow, t_e^\uparrow, t_e^\downarrow, t_h^\uparrow, t_h^\downarrow)^T$. However, the form of these expressions are very complex. For example, the expressions for the reflection coefficients can be written in the following from:

$$r_e^\uparrow = \frac{\omega_+^2 (R_1 R_2 - R_6 - R_7)}{\omega_+^2 P_4 (Q_7 Q_{10} \omega_- + R_7) (O_2 O_{15} P_3 R_9 - P_2 Q_1 Q_7 \omega_-) + \omega_+^2 R_1 R_{14}}, \quad (A1)$$

$$r_e^\downarrow = \frac{R_{15} + \omega_+ P_4^2 R_8 R_{13}}{\omega_+^2 P_4 (Q_7 Q_{10} \omega_- + R_7) (O_2 O_{15} P_3 R_9 - P_2 Q_1 Q_7 \omega_-) + \omega_+^2 R_1 R_{14}}, \quad (A2)$$

$$r_h^\uparrow = \frac{R_9 - R_{10} - R_{16} - R_{17}}{\omega_+^2 P_4 (Q_7 Q_{10} \omega_- + R_7) (O_2 O_{15} P_3 R_9 - P_2 Q_1 Q_7 \omega_-) + \omega_+^2 R_1 R_{14}}, \quad (A3)$$

$$r_h^\downarrow = \frac{R_{12} - R_{19} + \omega_+^2 P_4 R_8 (R_{11} - R_{18})}{\omega_+^2 P_4 (Q_7 Q_{10} \omega_- + R_7) (O_2 O_{15} P_3 R_9 - P_2 Q_1 Q_7 \omega_-) + \omega_+^2 R_1 R_{14}}, \quad (A4)$$

where we define,

$$\omega_\pm = \frac{u_\pm}{v_\pm},$$

$$\begin{aligned} O_1 &= p_3 - x_1, & O_2 &= p_1 - p_3, & O_3 &= x_5 - p_3, \\ O_4 &= p_3 - x_3, & O_5 &= p_2 - x_3, & O_6 &= p_2 - x_1, \\ O_7 &= p_2 - x_5, & O_8 &= p_4 - x_3, & O_9 &= p_4 - x_5, \\ O_{10} &= p_3 - x_5, & O_{11} &= p_3 + x_4, & O_{12} &= p_4 + x_4, \\ O_{13} &= p_2 + x_4, & O_{14} &= p_4 - x_1, & O_{15} &= x_5 - x_3, \end{aligned}$$

$$\begin{aligned} P_1 &= \beta y_1 - y_2, & P_2 &= \beta y_1 + y_3, & P_3 &= \beta y_3 - y_1, \\ P_4 &= \beta y_1 + y_2, & P_5 &= \beta y_2 + y_1, & P_6 &= \beta y_1 - y_3, \\ P_7 &= y_1 - \beta y_2, & P_8 &= y_1 - \beta y_3, & P_9 &= \beta y_3 + y_1, \end{aligned}$$

$$\begin{aligned} Q_1 &= O_3 x_3 \omega_+^2 + O_4 x_5 + p_1 \{p_3 (\omega_+^2 - 1) - x_5 \omega_+^2 + x_3\}, \\ Q_2 &= O_{10} x_4 \omega_+^2 + O_{11} x_5 + p_1 \{p_3 (\omega_+^2 - 1) - x_5 \omega_+^2 - x_4\}, \\ Q_3 &= -(\beta^2 - 1) y_2 y_1 + \beta y_1^2 - \beta y_2^2, \\ Q_4 &= \omega_- (O_3 x_1 \omega_+^2 + O_1 x_5 + p_1 \{p_3 (\omega_+^2 - 1) - x_5 \omega_+^2 + x_1\}), \\ Q_5 &= p_3 \{-2\beta p_4 (y_1^2 + y_2 y_3) + P_4 P_9 x_3 + P_1 P_3 (-x_5)\} \\ &\quad + p_4 (P_4 P_9 x_5 - P_1 P_3 x_3) - 2x_3 x_5 (y_1^2 + y_2 y_3), \\ Q_6 &= O_{10} O_{12} P_4 P_5 \omega_+ + O_9 O_{11} P_1 P_7 \omega_-, \\ Q_7 &= O_4 O_9 P_1 P_8 + O_8 O_{10} P_4 P_9, \\ Q_8 &= O_1 O_9 P_1 P_2 \omega_- - O_{14} O_{10} P_4 P_6 \omega_+, \\ Q_9 &= O_8 O_{11} P_7 P_9 \omega_- - O_4 O_{12} P_5 P_8 \omega_+, \\ Q_{10} &= -O_{11} O_7 P_1 P_5 - O_{13} O_{10} P_4 P_5 \omega_- \omega_+, \end{aligned}$$

$$\begin{aligned} R_1 &= Q_2 Q_3 Q_7 \omega_- - O_2 O_{15} P_4 P_3 Q_6, \\ R_2 &= Q_7 \omega_- (O_6 O_{10} P_4 P_6 \omega_- \omega_+ - O_1 O_7 P_1 P_2) \\ &\quad - Q_8 (O_4 O_7 P_1 P_3 - O_5 O_{10} P_4 P_9), \\ R_3 &= O_4 O_9 P_1 P_2 \omega_- - O_8 O_{10} P_4 P_6 \omega_+ + P_2 Q_1 Q_7 \omega_-, \\ R_4 &= O_4 O_9 P_1 P_2 \omega_-, \end{aligned}$$

$$\begin{aligned} R_5 &= O_2 O_{15} P_3 Q_8 + P_2 Q_4 Q_7, \\ R_6 &= Q_{10} Q_7 O_2 O_{15} P_3 Q_8 \omega_- - P_2 Q_4 Q_7, \\ R_7 &= -Q_6 (O_4 O_7 P_1 P_3 - O_5 O_{10} P_4 P_9), \\ R_8 &= R_1 R_2 \omega_+^2 + R_6 + R_7, \\ R_9 &= R_4 - O_8 O_{10} P_4 P_6 \omega_+, \\ R_{10} &= \frac{O_1 O_9 P_1 P_2 \omega_- - O_{14} O_{10} P_4 P_6 \omega_+}{Q_7 \omega_- \omega_+}, \\ R_{11} &= \frac{O_4 P_8 R_9}{O_{10} P_4 Q_7 \omega_- \omega_+} - \frac{O_4 P_2}{O_{10} P_4 \omega_+}, \\ R_{12} &= \frac{O_1 P_3}{O_{10} P_4 \omega_+} - \frac{O_4 P_8 Q_8}{O_{10} P_4 Q_7 \omega_- \omega_+}, \\ R_{13} &= -O_2 O_{15} P_3 R_3, \\ R_{14} &= Q_7 \omega_- (O_5 O_{10} P_4 P_6 \omega_- \omega_+ - O_4 O_7 P_1 P_2) \\ &\quad - R_9 (O_4 O_7 P_1 P_3 - O_5 O_{10} P_4 P_9), \\ R_{15} &= -\frac{P_4 R_5}{P_4 Q_6 R_{13} R_8 \omega_+}, \\ R_{16} &= \frac{P_4 Q_6 R_5}{R_1 Q_7 \omega_-}, \\ R_{17} &= \frac{P_4 Q_6 R_5}{Q_7 R_1 \omega_- \omega_+}, \\ R_{18} &= \frac{P_4 Q_9 R_{13}}{Q_5 R_1 \omega_- \omega_+}, \\ R_{19} &= \frac{P_4 Q_9 R_5}{Q_5 R_1 \omega_- \omega_+}, \end{aligned}$$

$$\begin{aligned} \beta &= e^{-i\phi}, \\ x_1 &= k_F^+ \cos \theta_F - 2iU_{int}, \\ x_2 &= k_F^- \cos \theta_F - 2iU_{int}, \\ x_3 &= k_F^+ S_1 - 2iU_{int}, \\ x_4 &= k_F^- S_2 + 2iU_{int}, \\ x_5 &= k_F^- S_2 - 2iU_{int}, \\ p_1 &= \lambda \cos \theta_e, & p_2 &= \lambda \cos \theta_e, \\ p_3 &= \lambda \cos \theta_h, & p_4 &= \lambda \cos \theta_h, \\ y_1 &= \cos \theta_m, & y_2 &= \sin \theta_m e^{i\chi_m}, & y_3 &= \sin \theta_m e^{-i\chi_m}. \end{aligned}$$

[1] S.S. Saxena, et al., Nature (London) **406**, 587 (2005).
[2] D. Aoki, et al., Nature (London) **413**, 613 (2001).
[3] C. Pfleiderer et al., Nature (London) **412**, 58 (2001).
[4] N.T. Huy et al., Phys. Rev. Lett. **99**, 067006 (2007).
[5] A.I. Buzdin, Rev. Mod. Phys. **77**, 935 (2005).
[6] I. Zutic, J. Fabian and S. Das. Sarma, Rev. Mod. Phys. **76**, 323 (2004).
[7] E. Bauer, et al., Phys. Rev. Lett. **92**, 027003 (2004).
[8] E. Bauer, I. Bonalde, and M. Sigris., Low Temp. Phys. **31**, 748 (2005).
[9] E. Bauer, et al., J. Phys.Soc. Jpn. **76**, 051009 (2007).

[10] G. Motoyama, et al., J. Phys. Conf. Ser. **400**, 022079 (2012).
[11] I. Kawasaki, et al., J. Phys. Soc. Jpn **82**, 084713 (2013).
[12] T. Akazawa, et al., J. Phys. Cond. Matter **16**, L29 (2009).
[13] V. K. Anand, et al., Phys. Rev. B. **83**, 064522 (2011).
[14] M. Smidman, et al., Phys. Rev. B. **89**, 094509 (2014).
[15] V. K. Anand, et al., Phys. Rev. B. **90**, 041513 (2014).
[16] K. Togano, et al., Phys. Rev. Lett. **93**, 247004 (2004).
[17] H. Q. Yuan, et al., Phys. Rev. Lett. **97**, 017006 (2006).
[18] P. Badica, et al., J. Phys. Soc. Jpn. **74**, 1014 (2005).
[19] B. T. Matthias, V. B. Compton and E. Corenzwit, J. Phys. Chem. Solids **19**, 130 (1961).

- [20] R. P. Singh, et al., Phys. Rev. Lett. **112**, 107002 (2014).
- [21] V. K. Pecharsky, L. L. Miller and K. A. Gschneidner, Phys. Rev. B **58**, 497 (1998).
- [22] A. D. Hillier, J. Quintanilla and R. Cywinski, Phys. Rev. Lett. **102**, 117007 (2009).
- [23] I. Bonalde et al., New J. Phys. **13**, 123022 (2011).
- [24] M. Yogi, et al., Phys. Rev. Lett. **93**, 027003 (2004).
- [25] M. N. Ali, et al., Phys. Rev. B **89**, 020505(R) (2014).
- [26] C. Q. Xu, et al., Phys. Rev. B **96**, 064528 (2017).
- [27] J. Flouquet and A. Buzdin, Phys. World **15**, 41 (2002).
- [28] S. Nandi et al., Phys. Rev. B. **89**, 014512 (2014).
- [29] L. P. Gor'kov, E. I. Rashba, Phys. Rev. Lett. **87**, 037004 (2001).
- [30] S. K. Yip, Phys. Rev. B **65**, 144508 (2002).
- [31] K. V. Samokhin, E. S. Zijlstra and S. K. Bose, Phys. Rev. B. **69**, 094514 (2004).
- [32] I. A. Sergienko and S. H. Curnoe, Phys. Rev. B. **70**, 214510 (2004).
- [33] P. A. Frigeri, D. F. Agterberg, A. Koga, and M. Sigrist, Phys. Rev. Lett. **92**, 097001 (2004).
- [34] S. Fujimoto, Phys. Rev. B **72**, 024515 (2005).
- [35] S. Fujimoto, J. Phys. Soc. Jpn. **76**, 051008 (2007).
- [36] W. Molenkamp, G. Schimdt and G. E. W. Bruer, Phys. Rev. B **64**, 121202(R) (2001).
- [37] S. Wu, K.V. Samokhin, Phys. Rev. B **82**, 184501 (2010).
- [38] S. Wu, K.V. Samokhin, Phys. Rev. B **81**, 214506 (2010).
- [39] E. Bauer, et al., Phys. Rev. B **80**, 064504 (2009).
- [40] K. Wakui, et al., J. Phys. Soc. Jpn. **78**, 034710 (2009).
- [41] R. L. Ribeiro, et al., J. Phys. Soc. Jpn. **78**, 115002 (2009).
- [42] P. K. Biswas, et al., Phys. Rev. B **84**, 184529 (2011).
- [43] S. Kuroiwa, et al., Phys. Rev. Lett. **100**, 097002 (2008).
- [44] J. Chen, et. al, Phys. Rev. B **83**, 144529 (2011).
- [45] J. Chen, et al., New J. Phys. **15**, 053005 (2013).
- [46] J. Linder and A. Sudbo, Phys. Rev. B **75**, 134509 (2007).
- [47] M. Bozovic and Z. Radovic, Phys. Rev. B. **66**, 134524 (2002).
- [48] M. Bozovic and Z. Radovic, New J. Phys. **9**, 264 (2007).
- [49] I. Zutic and O. T. Valls, Phys. Rev. B **60**, 6320 (1999).
- [50] I. Zutic and O. T. Valls, Phys. Rev. B **61**, 1555 (2000).
- [51] Q. Cheng, D. Yu and B. Jin, Phys Lett. A **378**, 2900 (2014).
- [52] Q. Cheng, B. Jin and D. Yu, Phys Lett. A **379**, 1172 (2015).
- [53] Y. Tanaka and S. Kashiwaya, Phys. Rev. Lett. **74**, 3541 (1995).
- [54] J. Linder and A. Sudbo, Phys. Rev. B **76**, 054511 (2007).
- [55] C. Iniotakis, et al., Phys. Rev. B **76**, 012501 (2007).
- [56] S. Kashiwaya, et al., Phys. Rev. B **60**, 3572 (1999).
- [57] N. Banerjee, et al., Nature Communications (London) **5**, 4048 (2014).
- [58] S. Acharjee and U. D. Goswami, J. Appl. Phys. **120**, 263902 (2016).
- [59] G.E. Blonder, M. Tinkham, T.M. Klapwijk, Phys. Rev. B **25**, 4515 (1982).
- [60] P.Kapri and S. Basu, Eur. Phys. J. B. **90**, 33 (2017).